npj | Quantum Materials

www.nature.com/npjquantmats

ARTICLE OPEN

Real-space anisotropy of the superconducting gap in the charge-density wave material 2H-$NbSe_2$

Antonio Sanna[1]✉, Camilla Pellegrini[2], Eva Liebhaber[3], Kai Rossnagel[4,5], Katharina J. Franke[3] and E. K. U. Gross[6]

We present a scanning tunneling microscopy (STM) and ab-initio study of the anisotropic superconductivity of 2H-$NbSe_2$ in the charge-density-wave (CDW) phase. Differential-conductance spectra show a clear double-peak structure, which is well reproduced by density functional theory simulations enabling full **k**- and real-space resolution of the superconducting gap. The hollow-centered (HC) and chalcogen-centered (CC) CDW patterns observed in the experiment are mapped onto separate van der Waals layers with different electronic properties. We identify the CC layer as the high-gap region responsible for the main STM peak. Remarkably, this region belongs to the same Fermi surface sheet that is broken by the CDW gap opening. Simulations reveal a highly anisotropic distribution of the superconducting gap within single Fermi sheets, setting aside the proposed scenario of a two-gap superconductivity. Our results point to a spatially localized competition between superconductivity and CDW involving the HC regions of the crystal.

npj Quantum Materials (2022)7:6 ; https://doi.org/10.1038/s41535-021-00412-8

INTRODUCTION

Collective phenomena such as superconductivity and charge- or spin-density modulations have been found to co-exist in many materials, the interplay among these correlations being discussed in terms of their competition or mutual enhancement[1–22]. The layered transition-metal dichalcogenide 2H-$NbSe_2$ is a prominent example undergoing a transition into a charge-ordered phase at $T \leq 33$ K, and into the superconducting phase at $T_c \leq 7.2$ K. Both orderings are driven by electron-phonon coupling[23–31] with a strong momentum dependence[14,17,20,32]. The superconducting gap turns out to have an anisotropic distribution over the Fermi surface (FS), whereby $NbSe_2$ has been interpreted either as a multigap or a highly anisotropic superconductor[32–36].

A clear understanding of the structure of the superconducting gap is indeed presently missing, and is one of the key unsolved questions about $NbSe_2$. Knowing whether superconducting anisotropy favors the stability of the superconducting state (like, e.g., in MgB_2) is interesting on itself. More importantly, accessing the momentum-dependent structure of the superconducting gap in the CDW phase would allow one to unveil the link between superconducting condensation and CDW ordering in this material, resolving the long-standing debate on their competition.

In this paper, we present clear evidence of anisotropic superconductivity in $NbSe_2$ by measuring the tunneling density of states (DOS) with unprecedented resolution combined with state-of-the-art first-principles simulations of the superconducting state based on density functional theory for superconductors (SCDFT). We emphasize that, unlike conventional approaches to superconductivity[37–39], SCDFT does not rely on any empirical parameter, which allows us to elucidate the strength and distribution of the superconducting gap.

RESULTS

STM spectroscopy

An atomically resolved constant-current STM image is shown in Fig. 1a. Besides the atomic corrugation of the terminating Se layer, the image reveals the modulation of the local DOS imposed by the CDW. As the CDW is incommensurate with the atomic lattice, (periodicity $|\mathbf{q}_{\mathrm{CDW}}| \lesssim 2\pi/(3a)$, where a is the in-plane lattice constant), different local patterns appear across the surface. The area in the orange rectangle shows a triangular pattern as a result of the maximum of the CDW being centered on a hollow site (hollow-centered, HC pattern). This continuously transforms into the chalcogen-centered (CC) pattern highlighted in the blue rectangle. Differential-conductance (d*I*/d*V*) spectra in different regions of the CDW are shown in Fig. 1b (for more spectra, see Supplementary Notes 4–6). All spectra exhibit a fully gapped region flanked by a broad peak distribution in the range $2.1\ \mathrm{mV} < \Delta/e < 3.1\ \mathrm{mV}$, with peculiar intensity variations, which can only be resolved by employing a superconducting tip.

Simulations - structural and normal-state properties

The CDW instability is captured by density functional theory (DFT) calculations in the undistorted cell (Ω_1), where it manifests itself in imaginary phonon frequencies occurring over a broad range of momenta centered at $\mathbf{q}_{\mathrm{CDW}}$[40]. As discussed in[23,28,29], the CDW can not be viewed as a purely electronic Peierls' instability driven by FS nesting, but is instead a structural phase transition assisted by the enhancement of the electron-phonon coupling (EPC) at the characteristic wave vector. Additionally, the CDW transition temperature can be accurately reproduced in DFT calculations by including anharmonic effects in the lattice dynamics[41]. In this paper we carry out a DFT study of the superconducting state in the CDW phase, providing a first-principles interpretation of the STM data.

[1]Max-Planck-Institut für Mikrostrukturphysik, Weinberg 2, 06120 Halle, Germany. [2]Department of Physics and Geology, University of Perugia, Via Pascoli 33, 06123 Perugia, Italy. [3]Fachbereich Physik, Freie Universität Berlin, Arnimallee 14, 14195 Berlin, Germany. [4]Institut für Experimentelle und Angewandte Physik, Christian-Albrechts-Universität zu Kiel, 24098 Kiel, Germany. [5]Ruprecht-Haensel-Labor, Deutsches Elektronen-Synchrotron DESY, 22607 Hamburg, Germany. [6]Fritz Haber Center for Molecular Dynamics, Institute of Chemistry, The Hebrew University of Jerusalem, Jerusalem 91904, Israel. ✉email: sanna@mpi-halle.mpg.de

We approximated the incommensurate CDW vector by $\mathbf{q}_{CDW} = (1/3, 0, 0)2\pi/a$, performing simulations within a superstructure unit cell ($\Omega_{3\times3}$) $3\times3\times1$ times Ω_1. The CDW reconstruction was obtained by relaxing the lattice along the phonon instabilities until all the modes were stable in a $2\times2\times4$ **q**-grid of the $\Omega_{3\times3}$ cell.

We found that the CDW formation induces small-amplitude atomic displacements reducing the minimum Nb–Se distance by ~1.0%. Remarkably, the dynamically stable reconstruction that we predict has a unit cell with two crystallographically inequivalent $NbSe_2$ layers, L_1 and L_2. These are shown in Fig. 2c,d and correspond, respectively, to the HC and CC patterns observed in experiment. We note that the obtained structures closely resemble those suggested in refs. [17,18,42]. The calculated CDW stabilization energy is of 3.7 meV per formula unit.

The CDW distortion is expected to induce relatively small changes of the electronic structure. Figure 2a,b compares the computed band structure and electronic DOS in the presence of the CDW and in the undistorted system. The two DOSs differ mainly by a broad dip developing in the CDW state slightly above the Fermi level, such that the reduction in the DOS at the Fermi level (N_F) induced by the CDW is relatively small (about 10%). Due to the large size of the supercell used in the calculations (54 atoms), the BZ folding makes the band structure in the CDW state hard to interpret. We thus employed a technique of band unfolding[43,44] from the supercell BZ to the larger BZ of the Ω_1 unit cell. As one can see, the CDW and undistorted bands largely overlap. A closer inspection, however, reveals band gap openings at several points of the BZ path, especially along the **MK** line, as well as energy shifts at the **K** point throughout the entire valence-band width.

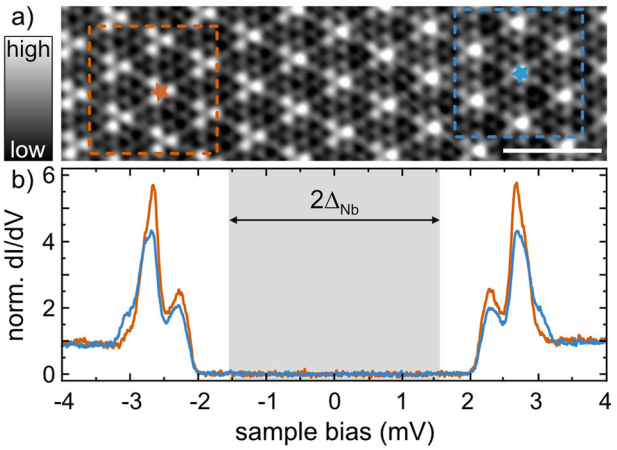

Fig. 1 Scanning tunneling microscopy measurements. a Constant-current image of a clean $NbSe_2$ surface (recorded with a Nb tip at a set point of 10 mV, 100 pA; the scale bar is 2 nm) to illustrate the smooth evolution of the CDW with respect to the atomic lattice. The frames highlight regions where the CDW maxima fall on a hollow site (orange) or on a Se atom (blue). **b** Differential-conductance d*I*/d*V* spectra taken at the positions indicated by stars in (**a**), recorded in constant-height mode (feedback was opened at the position of the blue spectrum for both traces with a set point of 5 mV, 250 pA and a modulation of 15 μV_{rms}).

The CDW effect on the electronic structure can be seen more clearly by considering a horizontal cut through the BZ. Fig. 3a shows the CDW reconstruction of the FS at $\mathbf{k}_z = 0$ obtained from the unfolding procedure. The unperturbed FS sheets (blue curves) are included for direct comparison. A double-walled cylindrical sheet of Nb 4d bands and a pocket of Se 4p character are centered at the **Γ** point. A second pair of Nb 4d-derived FS cylinders is located at the **K** point. This last double sheet appears to be significantly broader and blurred, indicating a stronger effect of the CDW distortion. Missing segments of the FS crossing the **MK** line, signal the openings of the CDW gap, which occur in excellent agreement with the ARPES measurements of refs. [32,45].

As already mentioned, the complexity of the CDW state is increased by the fact that the two structural layers undergo different reconstructions. To account for this aspect, we considered projections of the FS quasiparticle states onto the layers. Selected cuts of the unfolded projected FS are shown in Fig. 4. Most of the states (displayed in white) are found to span the entire crystal, yet a significant fraction is strongly localized on one layer. L_1 states are highlighted in red on the left panel of the figure, while L_2 states are shown in blue on the right. We observe significant differences: (i) On the $\mathbf{k}_z = 0$ plane, the FS of L_2 develops ring structures, unlike L_1. (ii) At $\mathbf{k}_z \simeq \frac{2}{3}\frac{\pi}{c}$ the inner **K**-centered sheet is mainly composed by L_2 states, whereas it has a stronger L_1 character on the **ΓKM** plane. (iii) By projecting the Fermi-pocket resolved DOS onto the layers,

$$N_F^{iD} = \sum_{n\mathbf{k}\in D} \delta(\varepsilon_{n\mathbf{k}}) P^i_{n\mathbf{k}}, \tag{1}$$

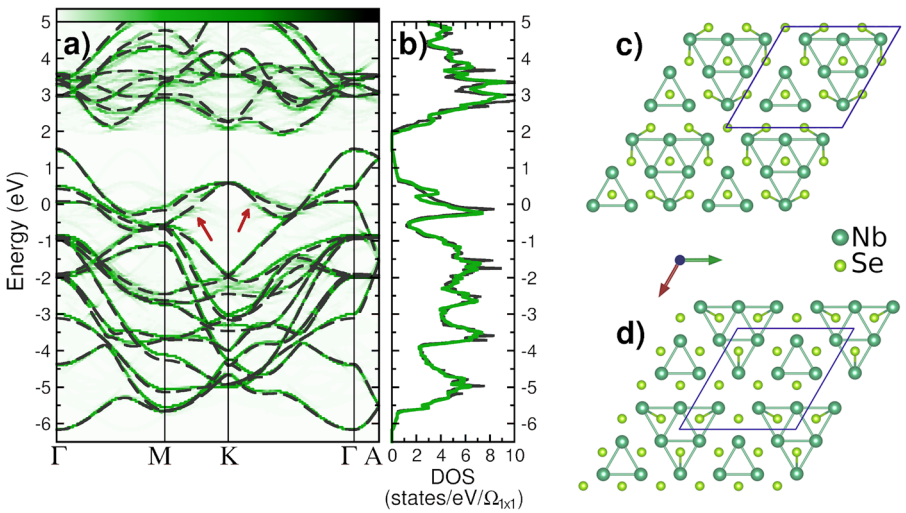

Fig. 2 Electronic properties and CDW structure. a Unfolded band structure and (**b**) electronic DOS of the CDW (green) and undistorted phase (black). CDW reconstruction of layers (**c**) L_2, chalcogen-centered pattern, and (**d**) L_1, hollow-centered pattern, in the $\Omega_{3\times3}$ unit cell (blue frame). The modulation of the atomic positions is highlighted by using a 2.53 Å cutoff for the plotted Nb–Se bond-sticks.

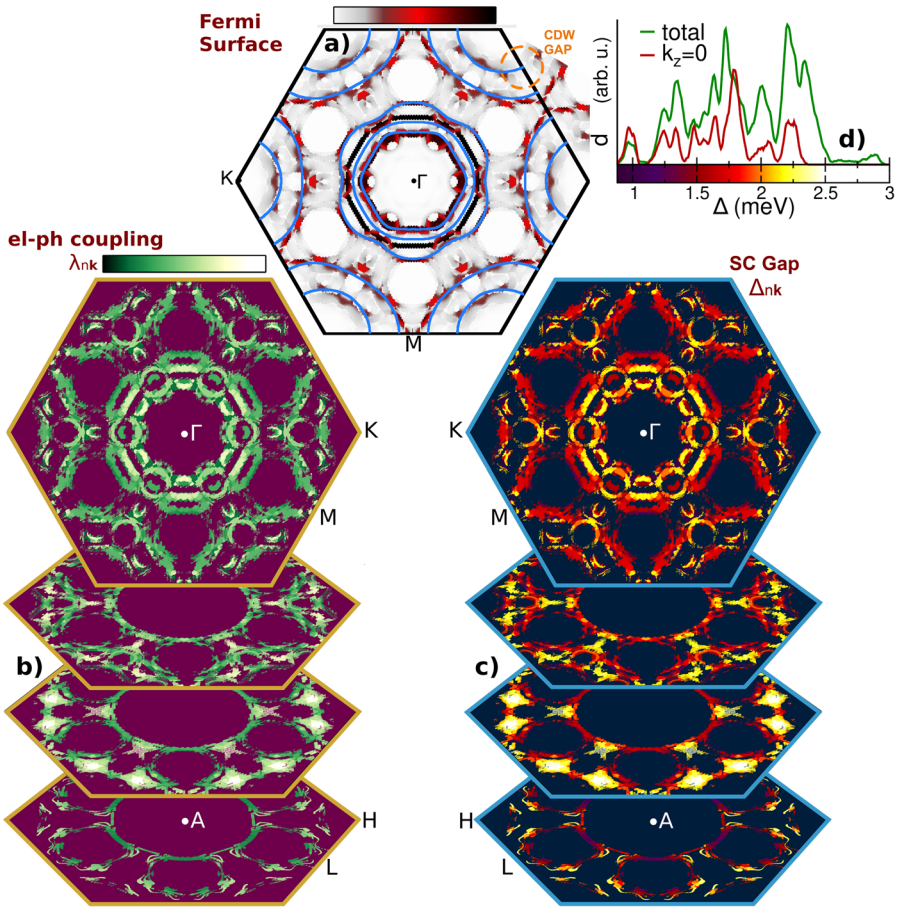

Fig. 3 Fermi surface anisotropy of the electron-phonon coupling and superconducting gap. a $\mathbf{k}_z = 0$ cut of the $NbSe_2$ Fermi surface obtained by unfolding the BZ. Color scale indicates the relative spectral weight. Blue curves represent the unperturbed FS sheets. **b** Electron–phonon coupling and (**c**) low-temperature superconducting gap computed in the unfolded BZ at random points on constant-$\mathbf{k}_z$ slices (of $0.1\frac{\pi}{c}$ width) and within ±0.1 mRy from the Fermi level. **d** Distribution of gap values computed over the full BZ (green) and the $|\mathbf{k}_z|<0.1\frac{\pi}{c}$ slice (red).

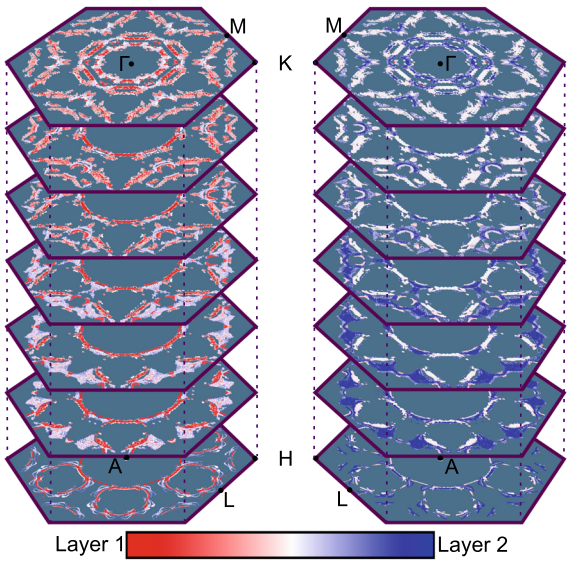

Fig. 4 Fermi surface projected on the structural layers. Slices of the unfolded Fermi surface computed at different values of $\mathbf{k}_z$ ($0.1\frac{\pi}{c}$ thick), from $\mathbf{k}_z = 0$ (top) to $\mathbf{k}_z = \pi/c$ (bottom), showing the projection of the electronic states onto the two structural layers L_1 and L_2. States localized on L_1 (L_2) are highlighted in red (blue).

Table 1. Layer and Fermi surface resolved electron–phonon parameters. Layer projections of **k**-partial integrals of the Fermi DOS (N_F^{iD}), electron–phonon coupling (λ^{iD}) and their ratio (V^{iD}), over the FS pockets at the **Γ** and **K** points ($i = L_1, L_2$; D indicates **Γ**- or **K**-centered sheets).

	Γ			K			Γ + K		
	N_F^{iD}	λ^{iD}	V^{iD}	N_F^{iD}	λ^{iD}	V^{iD}	N_F^{iD}	λ^{iD}	V^{iD}
L_1	0.62	0.19	0.30	1.16	0.40	0.34	1.78	0.58	0.33
L_2	0.74	0.23	0.32	1.56	0.61	0.39	2.30	0.84	0.37
$L_1 + L_2$	1.36	0.42	0.31	2.72	1.00	0.37	4.08	1.42	0.35

where $P^i_{n\mathbf{k}}$ is a projection operator with $i = L_1, L_2$, and D refers to **Γ**- or **K**-centered sheets, we found that, remarkably, $N_F^{L_1\Gamma}$ and $N_F^{L_1\mathbf{K}}$ are equally affected by the CDW (being reduced by 20%), whereas the DOS of L_2 stays almost constant. The calculated values of N_F^{iD} are listed in Table 1.

The CDW modulation can strongly affect the lattice dynamics and, in turn, influence phonon-driven superconductivity in complex ways. In principle, the CDW can co-exist with and even enhance superconductivity. This latter scenario, in particular, has been put forth by recent experimental findings[2–7,11,14–16,19,21,22,32]. As a first step to clarify the CDW effect on the superconducting

properties of $NbSe_2$, we simulated the lattice dynamics in the CDW phase. We point out that this is a computationally demanding task because of the large size of the crystallographic unit cell and the accuracy required in simulating the small CDW distortion.

We found that the phonon DOSs in the CDW and undistorted structure have a very similar shape. The unstable phonon mode, appearing with imaginary frequency in the latter, has, in fact, low spectral weight. Nevertheless, the CDW transition significantly alters the EPC: since the EPC strength, $\left|g^{\nu}_{n\mathbf{k}n'\mathbf{k}'}\right|^2$, is inversely proportional to the phonon frequency[37,46,47], a dynamical instability of the lattice shows up in a divergence of the coupling. The calculated $\alpha^2F(\omega)$ for the dynamically stable $3\times3\times1$ CDW structure (shown in Supplementary Note 1) gives a total EPC of $\lambda = 1.4$, placing $NbSe_2$ in the strong-coupling regime.

To assess the momentum anisotropy of the EPC, we calculated the **k**-resolved EPC parameters

$$\lambda_{n\mathbf{k}} = 2\sum_{n'\mathbf{q},\nu}\frac{\left|g^{\nu}_{n\mathbf{k}n'\mathbf{k}+\mathbf{q}}\right|^2}{\omega_{\nu\mathbf{q}}}\delta\left(\varepsilon_{n'\mathbf{k}+\mathbf{q}}\right). \tag{2}$$

The values obtained for the unfolded $\mathbf{k}_z = 0$ plane of the BZ are presented in Fig. 3b, where one can observe a complex pattern of hot spots (light) and weak-coupling (dark) regions. For a quantitative analysis, we examined the EPC contributions to **Γ**- and **K**-centered sheets arising from the two structural layers,

$$\lambda^{iD} = \frac{1}{N_F}\sum_{n\mathbf{k}\in D}\lambda_{n\mathbf{k}}\delta(\varepsilon_{n\mathbf{k}})P^{i}_{n\mathbf{k}}, \tag{3}$$

and the corresponding DOS-independent parameters, $V^{iD} = \lambda^{iD}/N_F^{iD}$. The computed values of λ^{iD} and V^{iD} are collected in Table 1. Since V^{iD} varies from a minimum of 0.30 ($V^{L_1\mathbf{\Gamma}}$) to a maximum of 0.39 ($V^{L_2\mathbf{K}}$), we deduce that the layers contribute almost equally to the intrinsic coupling of the various FS pockets. λ^{iD} is then determined essentially by the value of the DOS at the Fermi level. We also note that the FS **K**-cylinder and the layer L_2 can be identified as the regions with higher Fermi DOS and EPC in momentum and real space, respectively.

Simulation of the superconducting state

We simulated the superconducting state from first principles using SCDFT[48–50] with the state-of-the-art SPG functional[51]. The implementation of the method allowed us to make fully anisotropic calculations of the superconducting gap in both reciprocal and real space[52]. The **k**-dependent SCDFT gap equation was solved on a mesh of random **k** points more densely distributed around the FS for higher accuracy (computational details are provided in Supplementary Note 2 and refs. [47,53]). The estimated T_c of 10.2 K, is to be compared with an experimental value $T_c^{exp} = 7.2$ K. Given the usual accuracy of SCDFT calculations (within ~20% of T_c), this error is likely to be ascribed to (i) the neglect of anharmonic corrections to the lattice dynamics, that are enhanced close to the CDW transition[41], or (ii) limits on the precision in computing phonon properties and dielectric screening imposed by the large size of the CDW cell (see Supplementary Note 2 for an extended discussion). Nevertheless, our prediction is fairly accurate compared to that from conventional Eliashberg theory in the μ^* approximation[39,54]. This, in fact, gives $T_c \simeq 16$ K under the usual assumption $\mu^* = 0.11$, while an exceedingly high value of the Coulomb pseudopotential ($\mu^* = 0.28$) is required to reproduce the experimental result. The improved SCDFT estimation of T_c comes from including Coulomb interactions fully ab initio, thus retaining the energy dependence of the screened electron-electron interaction matrix elements $V(\varepsilon_{n\mathbf{k}}, \varepsilon_{n\mathbf{k}'})$. In fact, our simulations show that the electronic states at the Fermi level are poorly screened, that is $\mu = N_F V(0,0)$ is large. Moreover, because of a different orbital character, these states weakly interact with those far from the Fermi level, yielding a weak reduction of the Coulomb pseudopotential (high μ^*)[55].

The computed superconducting state turns out to be extremely complex. Unlike MgB_2, which has sheet-dependent anisotropy, the superconducting gap in momentum space of $NbSe_2$, $\Delta_{n\mathbf{k}}$, varies considerably in magnitude both between sheets and within a single sheet. We also note that whereas anisotropic effects in MgB_2 enhance T_c[56–58], that of $NbSe_2$ stays almost constant if anisotropy is washed out. Nevertheless, the degree of gap anisotropy is of essential importance for understanding thermodynamic and spectroscopic properties[27,32,34,36,45,59–61]. Figure 3d shows the histograms of gap values

$$\mathrm{d}(\Delta) = \frac{1}{N_F}\sum_{n,\mathbf{k}}\delta(\Delta_{n\mathbf{k}} - \Delta)\delta(\varepsilon_{n\mathbf{k}}) \tag{4}$$

over the full BZ (green) and the $\mathbf{k}_z = 0$ cut of the FS (red). The total distribution reveals a spread of gap values with the main peak at 2.3 meV and several smaller structures at lower values of Δ. While mid- and low-energy features of the curve are well reproduced by the $\mathbf{k}_z = 0$ slice of the CDW BZ, the source of the peak can be identified with a hot spot in $\Delta_{n\mathbf{k}}$ at 2/3 of the **ML** line. The obtained average gap value is of $\bar{\Delta} = 1.85$ meV, corresponding to $2\bar{\Delta}/k_BT_c = 4.3$, which is in excellent agreement with experiments[59]. Our overestimation of T_c naturally leads to an overestimation of the gap. However, multiplying Δ by the factor T_c^{exp}/T_c, the estimated gap is rescaled in between 0.7 and 1.7 meV, which is close to the range seen in Fig. 1b and provided by ARPES measurements[33]. Figure 3c shows the unfolded gap structure on constant-$\mathbf{k}_z$ slices of the BZ. We see a complex pattern of superconducting gaps that, like for other anisotropic superconductors[62–64], mirrors the structure of the EPC (compare the $\mathbf{k}_z = 0$ slice with Fig. 3b). In the $\mathbf{k}_z = 0$ plane, a high-gap region can be identified with the inner FS sheet of Nb character around the **Γ** point, while the Fermi arcs at **K** have, on average, a much smaller superconducting gap. This observation agrees with the inverse correlation between superconducting and CDW gap suggested by ARPES measurements[32]. Nevertheless, as already mentioned, the FS **K**-cylinder largely contributes to the superconducting condensation energy due to the overall higher DOS (Table 1) and a significant increase in the gap at large $\mathbf{k}_z$ (see the slice at $\mathbf{k}_z = \frac{2}{3}\frac{\pi}{c}$).

DISCUSSION

For a direct comparison with the experiment, we simulated STM images of bulk $NbSe_2$ by a superconducting Nb tip using the SCDFT gap. Specifically, the superconducting DOS of the sample was computed locally at the tip position from the real-space projection of Eq. (4) (see Supplementary Note 3 for an extended discussion). Figure 5a shows the computational differential-conductance spectra of layer L_1, L_2 and the full bulk, compared to the experimental spectrum averaged over the sample surface. The tunneling conductance calculated at the points corresponding to the experimental positions in Fig. 1a is also included. The related histograms of gap values are presented in Fig. 5b. Additionally, Fig. 5c provides a real-space image of the superconducting gap from a side view (bottom) and through horizontal cuts on the Nb planes of L_1 and L_2 (top). Simulations show a strong variation of the tunneling conductance with the scanning position, especially between the layers. Due to the higher DOS at the Fermi level, L_2 has, in fact, a much larger average gap (see the high-energy peak in the distribution of gap values). Moreover, a double-peak structure is clearly visible in the differential conductance computed for L_2, whereas it almost disappears for L_1. Changes in the experimental spectra as a function of the tip position are much less pronounced, and two distinct peaks are always observed (see Fig. 1 and Supplementary Note 4). However, in comparing simulated and experimental spectra, one should

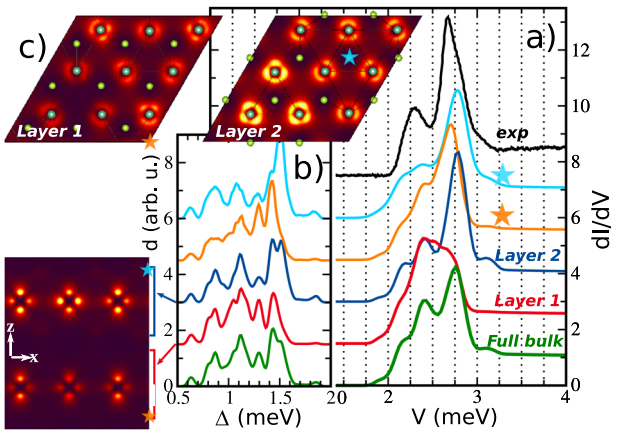

Fig. 5 Simulated real-space superconducting gap and STM spectra. a Simulated differential-conductance spectra of $NbSe_2$ for the bulk (green), layer L_1 (red), layer L_2 (dark blue) and at the experimental positions of Fig. 1a (orange, light blue). Experimental spectrum (black) obtained by averaging over multiple data traces as in Supplementary Fig. 4b. Tunneling currents are computed from the real-space distributions of gap values shown in (**b**), where Δ is scaled by the factor T_c^{exp}/T_c to correct for the overestimation of T_c. **c** Real-space view of the superconducting gap, showing stronger superconductivity on L_2, especially at specific Nb sites (bright spots).

consider that the actual CDW is slightly incommensurate, and that the structural patterns on L_1 and L_2 exist, in fact, on the same surface, smoothly transforming into each other[42]. This causes an additional degree of hybridization between the electronic states of the two layers, which is not accounted for in the simulations, as it would require using a prohibitively large cell. Additionally, simulations are done in the bulk, thus in absence of surface effects which may influence the gap anisotropy. Nevertheless, by comparing the black and green curves in Fig. 5, we see that the shape of the measured d*I*/d*V* tunneling spectrum is, overall, quite well reproduced, especially concerning the positions of the two peaks and the shoulder-like feature at ≈ 3 meV.

We mention that in a recent letter Heil and coworkers[65] used ab-initio Migdal–Eliashberg theory to simulate the superconducting properties and tunneling characteristics of NbS_2. While the tunneling spectra show strong similarities with those we predict and measure for $NbSe_2$, in the case of NbS_2 they are found to originate from a clear two-gap structure. If, on the one hand, these results demonstrate the importance of ab-initio methods for the interpretation of tunneling data, they also show that similar dichalcogenides can hide significantly different superconducting properties. It would be of interest to address this aspect by a detailed comparative ab-initio study.

To summarize, we presented high-resolution STM measurements of the differential conductance of $NbSe_2$ and an ab initio fully anisotropic description of the CDW and superconducting state. The agreement between measured and computed superconducting properties appears to be good. From our analysis emerge the following key aspects: (i) Contrary to the textbook case of MgB_2, the gap anisotropy does not influence the stability of the superconducting state, that is perturbations affecting the gap anisotropy are not expected to reduce T_c. (ii) The gap distribution on the FS shows rapid variations with **k** within each sheet. However, a high-gap structure can be clearly identified as responsible for the main STM coherence peak. Specifically, the peak originates from the same FS sheet that is broken by the occurrence of the CDW, i.e., the FS cylinder centered at the **K** point. (iii) HC regions of the crystal undergo a strong reduction of the Fermi DOS by the CDW, leading to a lower EPC compared to CC regions (whose Fermi DOS is almost unaffected).

Overall, our simulations indicate that superconducting and CDW orderings in $NbSe_2$ compete in HC regions, whereas superconductivity is not suppressed in CC regions. We rule out, however, a two-gap scenario, providing evidence of strong superconducting gap anisotropy.

METHODS

Crystal synthesis and characterization

Bulk crystals of $NbSe_2$ were grown by chemical vapor transport[32] and cleaved under ultra-high vacuum. Scanning tunneling microscopy and spectroscopy measurements were performed at 1.1 K with superconducting tips fabricated by indenting a clean NbTi wire into a Nb(111) crystal until the tip's energy gap reached the bulk value ($2\Delta_{tip} \approx 3.1$ meV). Since the probed signal is a convolution of the DOS of substrate and tip, all the measured spectral features of the sample are shifted by the tip's energy gap. Additionally, the differential-conductance signal is weighted by the energy-dependent tunneling probability.

Theoretical calculations

We calculated normal-state properties within DFT[66,67] using the local density approximation[68]. Atomic core states were treated in the norm-conserving pseudopotential approach as implemented in the Quantum Espresso code[69]. Phonon frequencies and EPC were computed by means of density functional perturbation theory[70] with an electronic temperature of 270 meV[40]. Further computational details are given in Supplementary Note 2.

DATA AVAILABILITY

The data that support the findings of this study are available from the corresponding author upon reasonable request.

Received: 23 July 2021; Accepted: 30 November 2021;
Published online: 14 January 2022

REFERENCES

1. da Silva Neto, E. H. et al. Ubiquitous interplay between charge ordering and high-temperature superconductivity in cuprates. *Science* **343**, 393–396 (2014).
2. Liu, Y. et al. Superconductivity induced by Se-doping in layered charge-density-wave system 1T−$TaS_{2-x}Se_x$. *Appl. Phys. Lett.* **102**, 192602 (2013).
3. Li, L. J. et al. Fe-doping-induced superconductivity in the charge-density-wave system 1T−TaS_2. *EPL* **97**, 67005 (2012).
4. Kusmartseva, A. F., Sipos, B., Berger, H., Forró, L. & Tutiš, E. Pressure induced superconductivity in pristine 1T−$TiSe_2$. *Phys. Rev. Lett.* **103**, 236401 (2009).
5. Joe, Y. I. et al. Emergence of charge density wave domain walls above the superconducting dome in 1T−$TiSe_2$. *Nat. Phys.* **10**, 421–425 (2014).
6. Bhoi, D. et al. Interplay of charge density wave and multiband superconductivity in 2H − Pd_xTaSe_2. *Sci. Rep.* **6**, 24068 (2016).
7. Morosan, E. et al. Superconductivity in Cu_xTiSe_2. *Nat. Phys.* **2**, 544–550 (2006).
8. Dai, P. Antiferromagnetic order and spin dynamics in iron-based superconductors. *Rev. Mod. Phys.* **87**, 855–896 (2015).
9. Manzeli, S., Ovchinnikov, D., Pasquier, D., Yazyev, O. V. & Kis, A. 2D transition metal dichalcogenides. *Nat. Rev. Mater.* **2**, 17033 (2017).
10. Chang, J. et al. Direct observation of competition between superconductivity and charge density wave order in $YBa_2Cu_3O_{6.67}$. *Nat. Phys.* **8**, 871–876 (2012).
11. Fujita, M., Goka, H., Yamada, K. & Matsuda, M. Competition between charge- and spin-density-wave order and superconductivity in $La_{1.875}Ba_{0.125-x}Sr_xCuO_4$. *Phys. Rev. Lett.* **88**, 167008 (2002).
12. Gabovich, A. M. et al. Competition of superconductivity and charge density waves in cuprates: recent evidence and interpretation. *Adv. Condens. Matter Phys.* **2010**, 1–40 (2010).
13. Gabovich, A. M., Voitenko, A. I., Annett, J. F. & Ausloos, M. Charge- and spin-density-wave superconductors. *Supercond. Sci. Technol.* **14**, R1–R27 (2001).
14. Kiss, T. et al. Charge-order-maximized momentum-dependent superconductivity. *Nat. Phys.* **3**, 720–725 (2007).
15. Xi, X. et al. Strongly enhanced charge-density-wave order in monolayer 2H −$NbSe_2$. *Nat. Nanotechnol.* **10**, 765–769 (2015).
16. Cho, K. et al. Using controlled disorder to probe the interplay between charge order and superconductivity in 2H−$NbSe_2$. *Nat. Commun.* **9**, 2796 (2018).

17. Lian, C.-S., Si, C. & Duan, W. Unveiling charge-density wave, superconductivity, and their competitive nature in two-dimensional 2H−$NbSe_2$. *Nano Lett.* **18**, 2924–2929 (2018).
18. Zheng, F. & Feng, J. Electron-phonon coupling and the coexistence of superconductivity and charge-density wave in monolayer $NbSe_2$. *Phys. Rev. B* **99**, 161119(R) (2019).
19. Soumyanarayanan, A. et al. Quantum phase transition from triangular to stripe charge order in $NbSe_2$. *Proc. Natl Acad. Sci.* **110**, 1623–1627 (2013).
20. Leroux, M. et al. Strong anharmonicity induces quantum melting of charge density wave in 2H−$NbSe_2$ under pressure. *Phys. Rev. B* **92**, 140303(R) (2015).
21. Ugeda, M. M. et al. Characterization of collective ground states in single-layer $NbSe_2$. *Nat. Phys.* **12**, 92–97 (2016).
22. Yang, Y. et al. Enhanced superconductivity upon weakening of charge density wave transport in 2H−TaS_2 in the two-dimensional limit. *Phys. Rev. B* **98**, 035203 (2018).
23. Weber, F. et al. Extended phonon collapse and the origin of the charge-density wave in 2H−$NbSe_2$. *Phys. Rev. Lett.* **107**, 107403 (2011).
24. Rossnagel, K. et al. Fermi surface of 2H−$NbSe_2$ and its implications on the charge-density-wave mechanism. *Phys. Rev. B* **64**, 235119 (2001).
25. Rossnagel, K. On the origin of charge-density waves in select layered transition-metal dichalcogenides. *J. Phys.: Condens. Matter* **23**, 213001 (2011).
26. Malliakas, C. D. & Kanatzidis, M. G. Nb-Nb interactions define the charge density wave structure of 2H−$NbSe_2$. *J. Am. Chem. Soc.* **135**, 1719–1722 (2013).
27. Valla, T. et al. Quasiparticle spectra, charge-density waves, superconductivity, and electron-phonon coupling in 2H−$NbSe_2$. *Phys. Rev. Lett.* **92**, 086401 (2004).
28. Johannes, M. D., Mazin, I. I. & Howells, C. A. Fermi-surface nesting and the origin of the charge-density wave in $NbSe_2$. *Phys. Rev. B* **73**, 205102 (2006).
29. Johannes, M. D. & Mazin, I. I. Fermi surface nesting and the origin of charge density waves in metals. *Phys. Rev. B* **77**, 165135 (2008).
30. Arguello, C. J. et al. Visualizing the charge density wave transition in 2H−$NbSe_2$ in real space. *Phys. Rev. B* **89**, 235115 (2014).
31. Zhu, X., Cao, Y., Zhang, J., Plummer, E. & Guo, J. Classification of charge density waves based on their nature. *Proc. Natl Acad. Sci.* **112**, 2367–2371 (2015).
32. Rahn, D. J. et al. Gaps and kinks in the electronic structure of the superconductor 2H−$NbSe_2$ from angle-resolved photoemission at 1 K. *Phys. Rev. B* **85**, 224532 (2012).
33. Yokoya, T. et al. Fermi surface sheet-dependent superconductivity in 2H−$NbSe_2$. *Science* **294**, 2518–2520 (2001).
34. Guillamon, I., Suderow, H., Guinea, F. & Vieira, S. Intrinsic atomic-scale modulations of the superconducting gap of 2H−$NbSe_2$. *Phys. Rev. B* **77**, 134505 (2008).
35. Noat, Y. et al. Quasiparticle spectra of 2H−$NbSe_2$: two-band superconductivity and the role of tunneling selectivity. *Phys. Rev. B* **92**, 134510 (2015).
36. Boaknin, E. et al. Heat conduction in the vortex state of $NbSe_2$: evidence for multiband superconductivity. *Phys. Rev. Lett.* **90**, 117003 (2003).
37. McMillan, W. L. Transition temperature of strong-coupled superconductors. *Phys. Rev.* **167**, 331–344 (1968).
38. Carbotte, J. P. Properties of boson-exchange superconductors. *Rev. Mod. Phys.* **62**, 1027–1157 (1990).
39. Allen, P. B. & Mitrović, B. *Theory of Superconducting T_c*, Vol. 37 of *Solid State Physics* (Academic Press, 1983).
40. Calandra, M., Mazin, I. I. & Mauri, F. Effect of dimensionality on the charge-density wave in few-layer 2H−$NbSe_2$. *Phys. Rev. B* **80**, 241108(R) (2009).
41. Bianco, R., Monacelli, L., Calandra, M., Mauri, F. & Errea, I. Weak dimensionality dependence and dominant role of ionic fluctuations in the charge-density-wave transition of $NbSe_2$. *Phys. Rev. Lett.* **125**, 106101 (2020).
42. Gye, G., Oh, E. & Yeom, H. W. Topological landscape of competing charge density waves in 2H−$NbSe_2$. *Phys. Rev. Lett.* **122**, 016403 (2019).
43. Medeiros, P. V. C., Stafström, S. & Björk, J. Effects of extrinsic and intrinsic perturbations on the electronic structure of graphene: retaining an effective primitive cell band structure by band unfolding. *Phys. Rev. B* **89**, 041407(R) (2014).
44. Medeiros, P. V. C., Tsirkin, S. S., Stafström, S. & Björk, J. Unfolding spinor wave functions and expectation values of general operators: introducing the unfolding-density operator. *Phys. Rev. B* **91**, 041116(R) (2015).
45. Borisenko, S. V. et al. Two energy gaps and Fermi-surface "arcs" in $NbSe_2$. *Phys. Rev. Lett.* **102**, 166402 (2009).
46. Giustino, F. Electron-phonon interactions from first principles. *Rev. Mod. Phys.* **89**, 015003 (2017).
47. Flores-Livas, J. A. et al. A perspective on conventional high-temperature superconductors at high pressure: methods and materials. *Phys. Rep.* **856**, 1–78 (2020).
48. Oliveira, L. N., Gross, E. K. U. & Kohn, W. Density-functional theory for superconductors. *Phys. Rev. Lett.* **60**, 2430–2433 (1988).
49. Lüders, M. et al. Ab initio theory of superconductivity. I. Density functional formalism and approximate functionals. *Phys. Rev. B* **72**, 024545 (2005).
50. Marques, M. A. L. et al. Ab initio theory of superconductivity. II. Application to elemental metals. *Phys. Rev. B* **72**, 024546 (2005).
51. Sanna, A., Pellegrini, C. & Gross, E. K. U. Combining Eliashberg theory with density functional theory for the accurate prediction of superconducting transition temperatures and gap functions. *Phys. Rev. Lett.* **125**, 057001 (2020).
52. Linscheid, A., Sanna, A., Floris, A. & Gross, E. K. U. First-principles calculation of the real-space order parameter and condensation energy density in phonon-mediated superconductors. *Phys. Rev. Lett.* **115**, 097002 (2015).
53. Sanna, A. In *The Physics of Correlated Insulators, Metals, and Superconductors* Vol. 7 Ch. 16, 429 (eds Pavarini, E., Koch, E., Scalettar, R., & Martin, R.) (Verlag des Forschungszentrum Jülich, 2017).
54. Scalapino, D. J., Schrieffer, J. R. & Wilkins, J. W. Strong-coupling superconductivity. I. *Phys. Rev.* **148**, 263–279 (1966).
55. Morel, P. & Anderson, P. W. Calculation of the superconducting state parameters with retarded electron-phonon interaction. *Phys. Rev.* **125**, 1263–1271 (1962).
56. An, J. M. & Pickett, W. E. Superconductivity of MgB_2: covalent bonds driven metallic. *Phys. Rev. Lett.* **86**, 4366–4369 (2001).
57. Floris, A. et al. Superconducting properties of MgB_2 from first principles. *Phys. Rev. Lett.* **94**, 037004 (2005).
58. Putti, M. et al. Intraband vs. interband scattering rate effects in neutron irradiated MgB_2. *EPL* **77**, 57005 (2007).
59. Huang, C. L. et al. Experimental evidence for a two-gap structure of superconducting $NbSe_2$: a specific-heat study in external magnetic fields. *Phys. Rev. B* **76**, 212504 (2007).
60. Fletcher, J. D. et al. Penetration depth study of superconducting gap structure of 2H−$NbSe_2$. *Phys. Rev. Lett.* **98**, 057003 (2007).
61. Zehetmayer, M. & Weber, H. W. Experimental evidence for a two-band superconducting state of $NbSe_2$ single crystals. *Phys. Rev. B* **82**, 014524 (2010).
62. Sanna, A. et al. Anisotropic gap of superconducting CaC_6: a first-principles density functional calculation. *Phys. Rev. B* **75**, 020511(R) (2007).
63. Floris, A., Sanna, A., Massidda, S. & Gross, E. K. U. Two-band superconductivity in Pb from ab initio calculations. *Phys. Rev. B* **75**, 054508 (2007).
64. Profeta, G. et al. Superconductivity in lithium, potassium, and aluminum under extreme pressure: A first-principles study. *Phys. Rev. Lett.* **96**, 047003 (2006).
65. Heil, C. et al. Origin of superconductivity and latent charge density wave in NbS_2. *Phys. Rev. Lett.* **119**, 087003 (2017).
66. Kohn, W. & Sham, L. J. Self-consistent equations including exchange and correlation effects. *Phys. Rev.* **140**, A1133–A1138 (1965).
67. Hohenberg, P. & Kohn, W. Inhomogeneous electron gas. *Phys. Rev.* **136**, B864–B871 (1964).
68. Perdew, J. P. & Zunger, A. Self-interaction correction to density-functional approximations for many-electron systems. *Phys. Rev. B* **23**, 5048–5079 (1981).
69. Giannozzi, P. et al. Quantum espresso: a modular and open-source software project for quantum simulations of materials. *J. Phys.: Condens. Matter* **21**, 395502 (2009).
70. Baroni, S., de Gironcoli, S., Dal Corso, A. & Giannozzi, P. Phonons and related crystal properties from density-functional perturbation theory. *Rev. Mod. Phys.* **73**, 515–562 (2001).

ACKNOWLEDGEMENTS

The authors acknowledge financial support by the European Research Council Advanced Grant FACT (ERC-2017-AdG-788890), the CarESS project, Deutsche Forschungsgemeinschaft through grant CRC 183 (project C03), and the European Research Council through the consolidator grant "NanoSpin".

AUTHOR CONTRIBUTIONS

K.R. provided the samples. E.L. and K.J.F. performed the STM characterization and related analysis. A.S and C.P. performed ab-initio simulations and their analysis. A.S., C.P., E.L., K.R., K.J.F., and E.K.U.G. contributed to the discussion and writing of the manuscript.

FUNDING

Open Access funding enabled and organized by Projekt DEAL.

COMPETING INTERESTS

The authors declare no competing interests.

ADDITIONAL INFORMATION

Supplementary information The online version contains supplementary material available at https://doi.org/10.1038/s41535-021-00412-8.

Correspondence and requests for materials should be addressed to Antonio Sanna.

Reprints and permission information is available at http://www.nature.com/reprints

Publisher's note Springer Nature remains neutral with regard to jurisdictional claims in published maps and institutional affiliations.